Electronic Supplementary Information

Superior metal storage properties of Zn-containing porous carbon nanostructures for Na and Li metal batteries

Kyungbae Kim,[a] Seunghwan Jeon,[b] Han-Seul Kim,[a] Hyungeun Seo,[a] Hyun-seung Kim,[b] Marca M. Doeff,[c] Sang-Gil Woo*[b] and Jae-Hun Kim*[a]

[a]School of Materials Science and Engineering, Kookmin University, Seoul 02707, Republic of Korea. E-mail: jaehunkim@kookmin.ac.kr

[b]Advanced Batteries Research Center, Korea Electronics Technology Institute, Seongnam, Gyeonggi 13509, Republic of Korea. E-mail: blackdragon@keti.re.kr

[c]Energy Storage and Distributed Resources Division, Lawrence Berkeley National Laboratory, Berkeley, CA 94720, USA

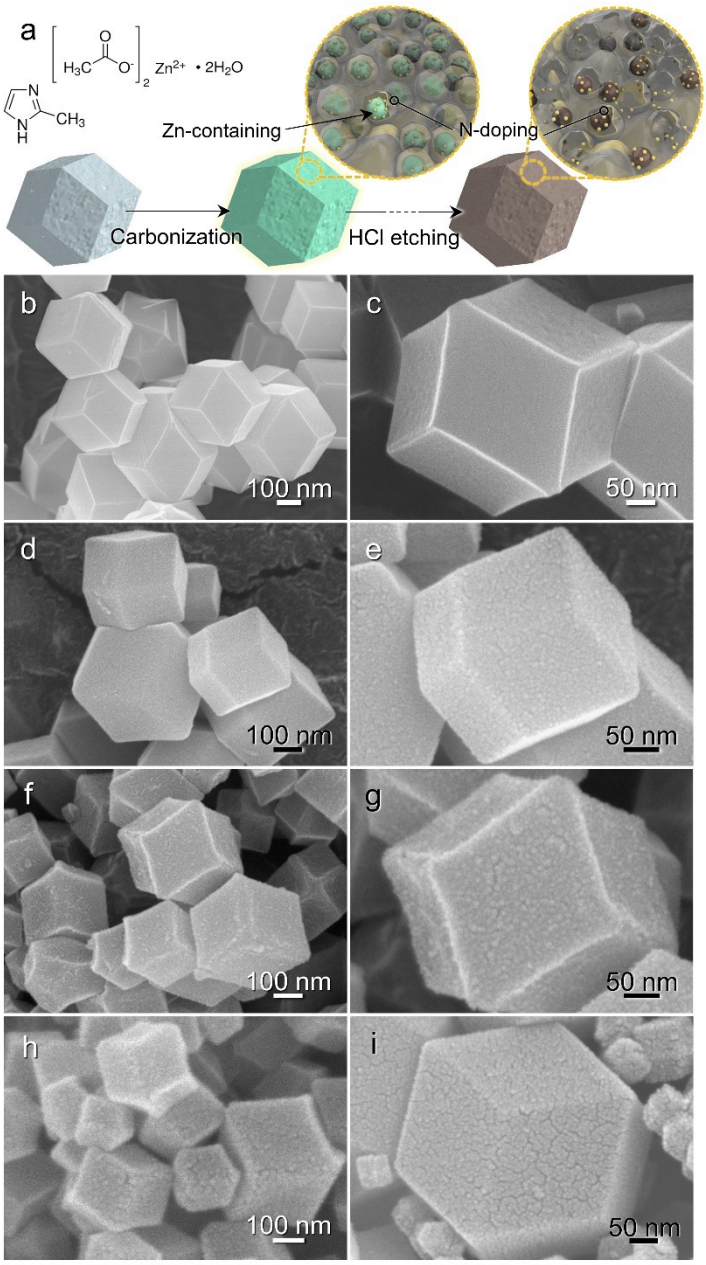

Fig. S1. (a) Synthesis method of the Zn-containing porous carbon materials and FE-SEM images: (b, c) as-prepared ZIF-8, (d, e) HZPC, (f, g) MZPC, and (h, i) LZPC.

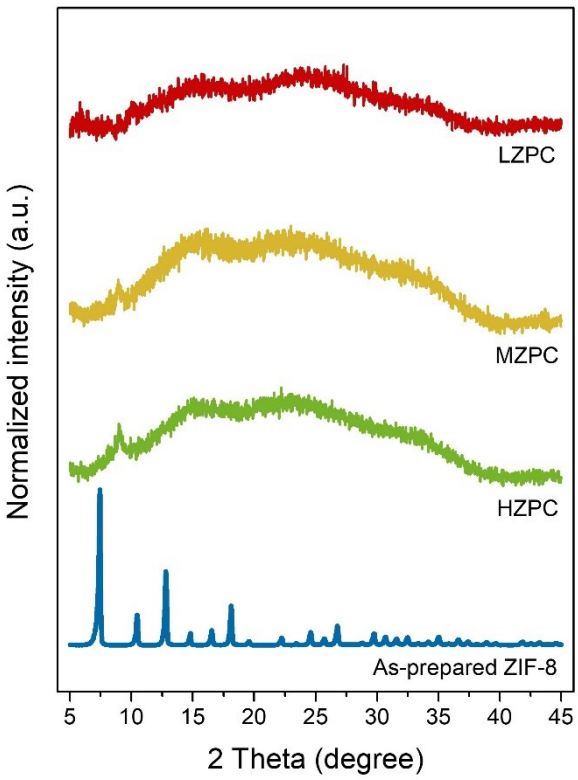

Fig. S2. XRD patterns of as-prepared ZIF-8 and Zn-containing porous carbon materials.

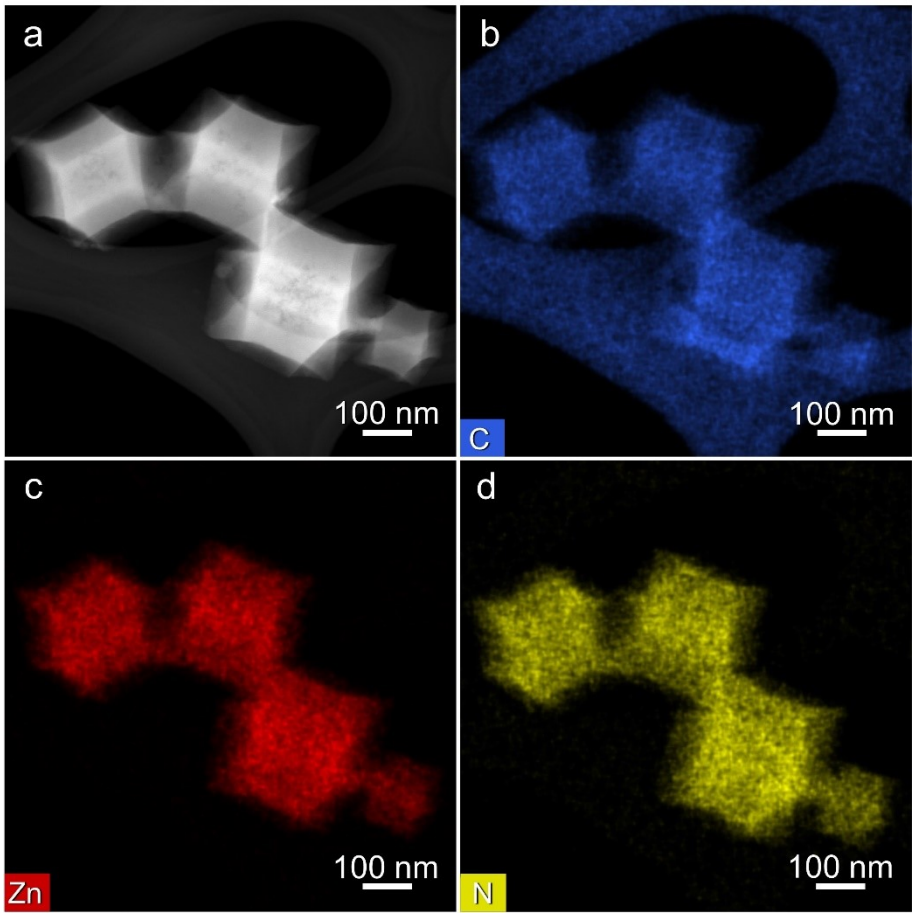

Fig. S3. STEM image and EDS elemental mapping images of the HZPC sample.

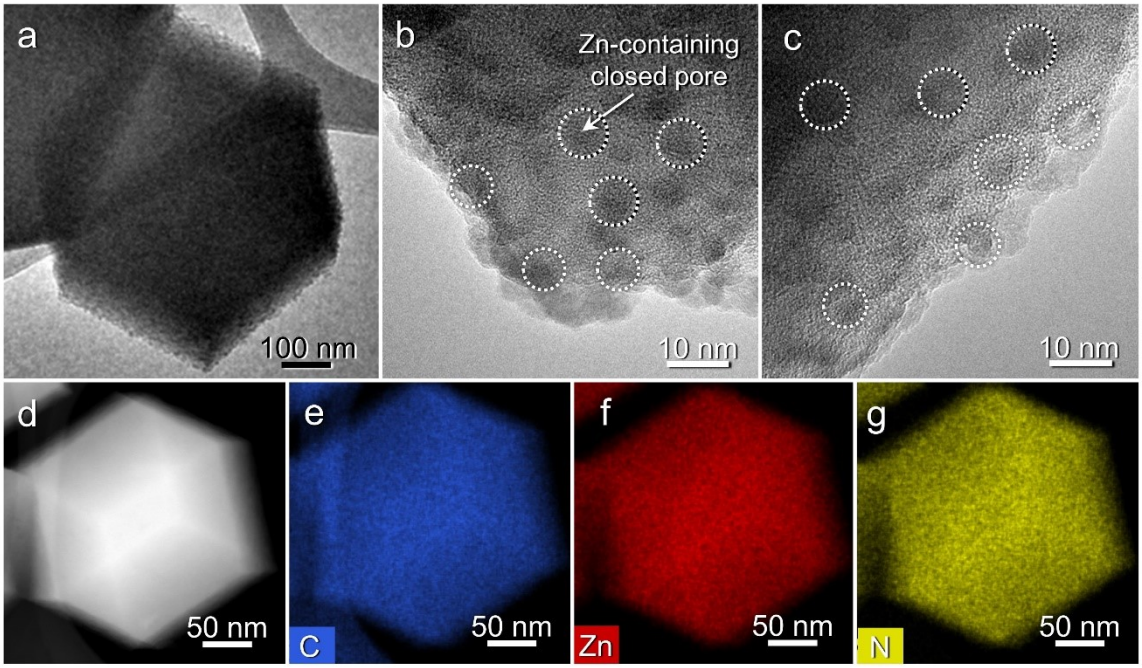

Fig. S4. Morphological characterization of MZPC: (a–c) HR-TEM images showing the porous surface structure and (d–g) FE-SEM and EDS elemental mapping images corresponding to C, Zn, and N elements.

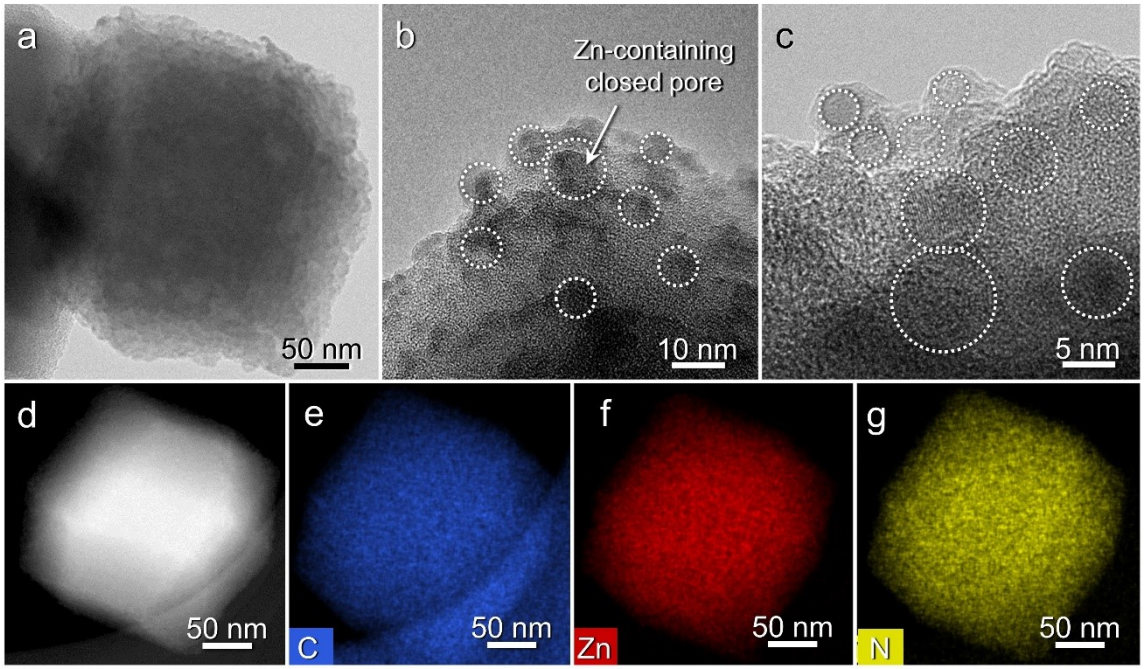

Fig. S5. Morphological characterization of LZPC: (a–c) HR-TEM images showing the porous surface structure and (d–g) FE-SEM and EDS elemental mapping images corresponding to C, Zn, and N elements.

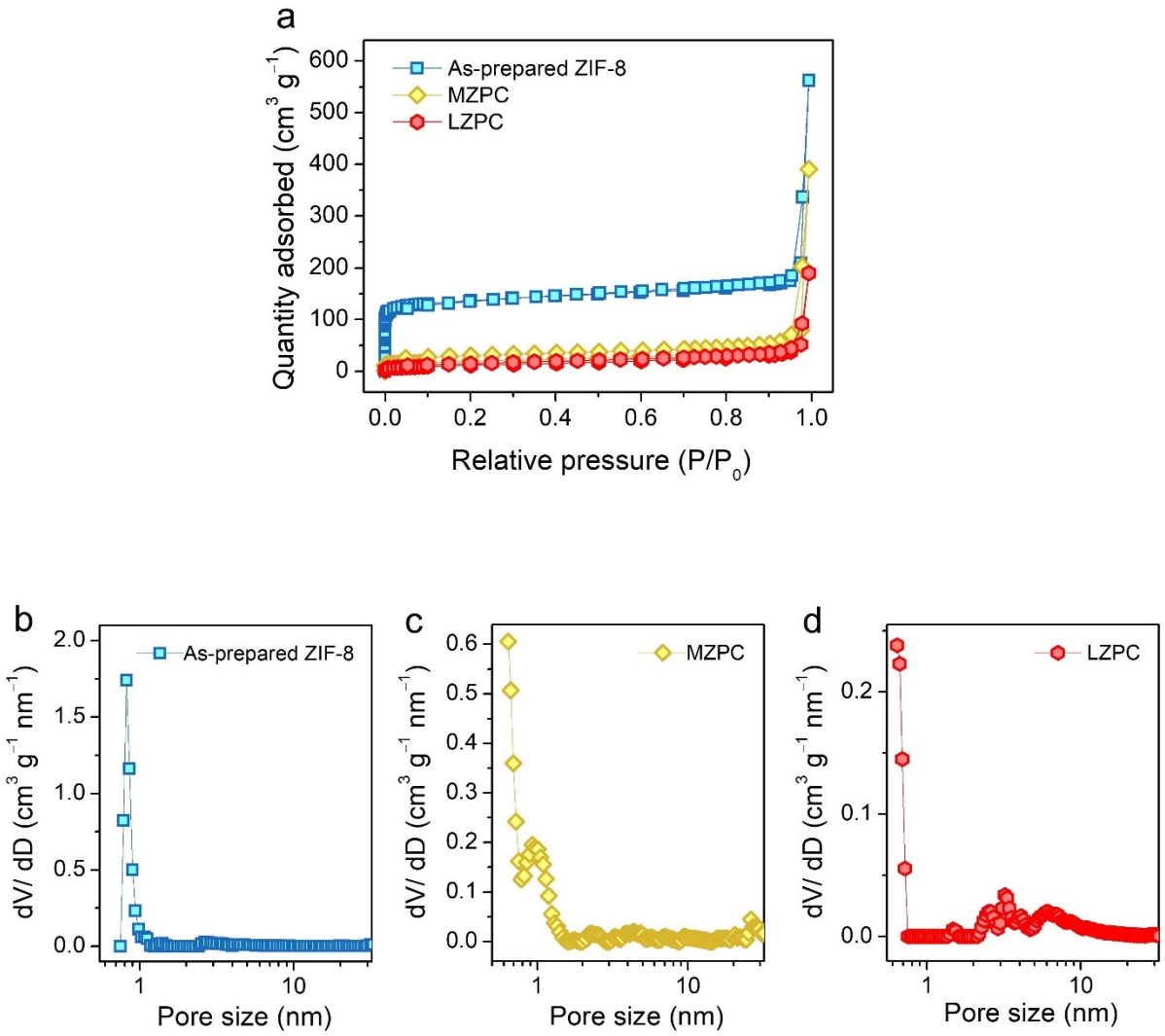

Fig. S6. (a) Nitrogen adsorption-desorption isotherms and (b–d) pore size distribution of ZIF-8, MZPC, and LZPC.

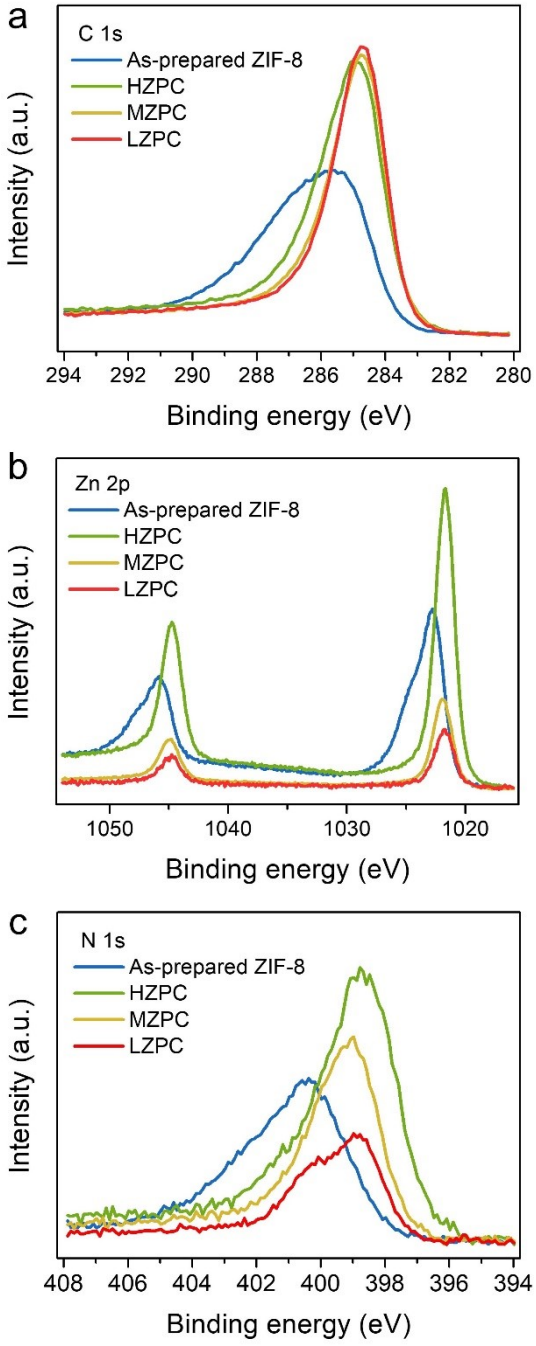

Fig. S7. XPS core-level spectra of all samples: (a) C 1s, (b) Zn 2p, and (c) N 1s. The XPS signals were obtained after Ar etching for 600 s.

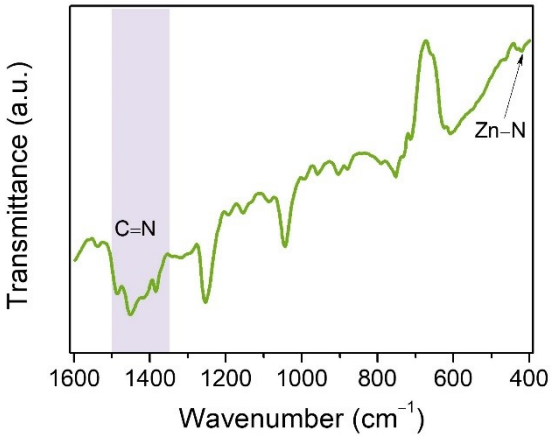

Fig. S8. FT-IR spectrum of HZPC.

Table S1. Electrical conductivity measurement results of the HZPC, MZPC, LZPC, and bare Cu foil electrodes.

Materials	HZPC	MZPC	LZPC	Cu foil
Resistivity (Ωm)	1.97×10^{-8}	2.98×10^{-8}	4.73×10^{-8}	1.71×10^{-8}
Conductivity (S cm^{-1})	5.07×10^{5}	3.36×10^{5}	2.11×10^{5}	5.84×10^{5}

The resistance of the electrodes was measured by using a four-point linear scan voltammetry method (Biologic VSP potentiostat). The electrical conductivity (σ) of the electrode can be determined using the equation below with the measured resistance:

$$\sigma = \frac{1}{\rho} = \frac{1}{RA}l$$

R is the measured resistance. l and A are length and cross-sectional area of the sample, respectively. The strip-type electrode (length: 3 cm) was used. The electrical conductivity of the bare Cu foil was calculated to be 5.84×10^{5} S cm^{-1}, which is the highest in the electrodes because it is pure metal. Among the porous carbon electrodes including the Cu foil current collector, HZPC exhibited the highest electrical conductivity of 5.07×10^{5} S cm^{-1}, which can be attributed to the high Zn content in the sample.

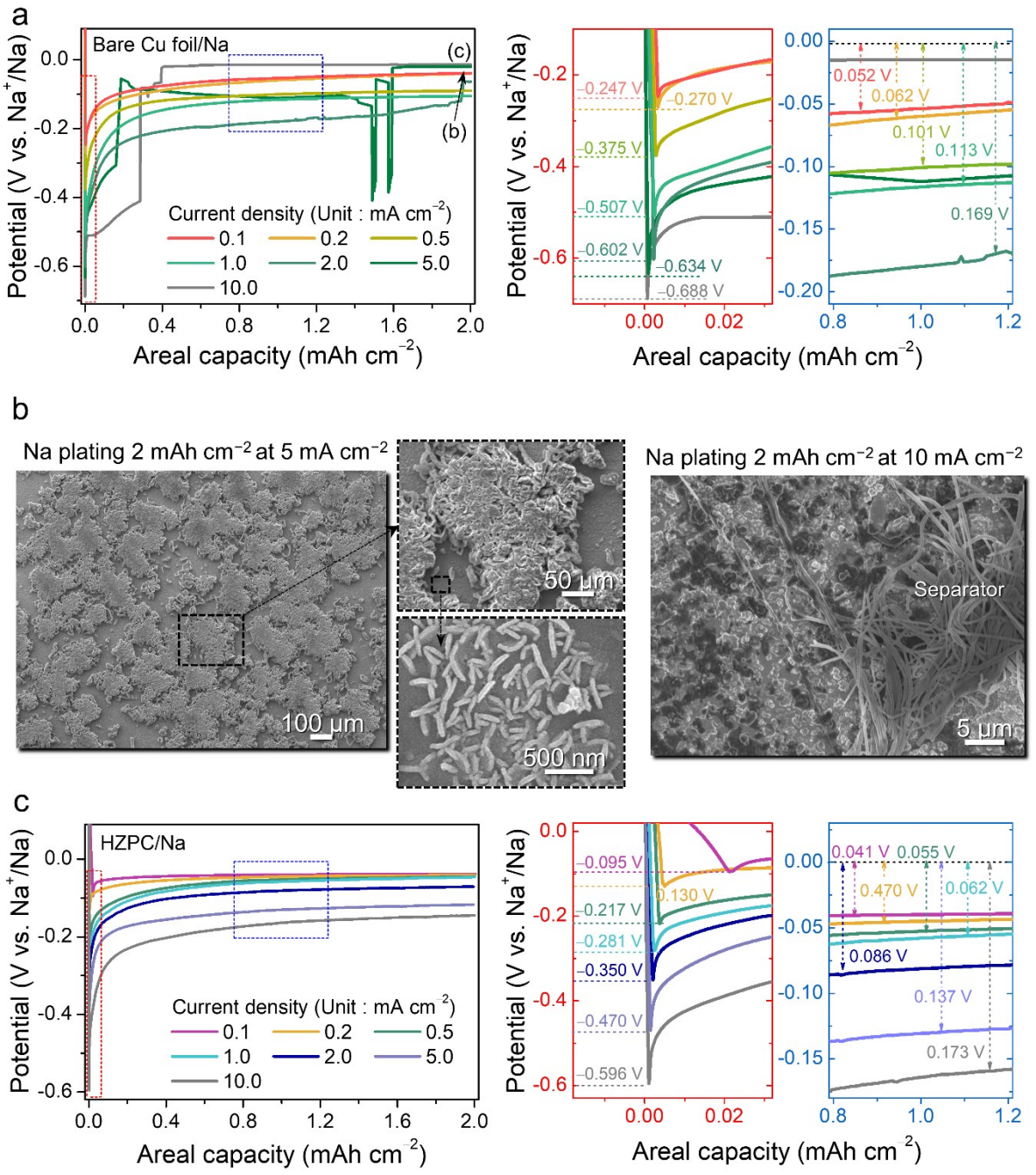

Fig. S9. (a) Voltage profiles of the bare Cu foil electrode for the first Na deposition at current densities from 0.1 to 10.0 mA cm^{-1}, (b) FE-SEM images after the first deposition at current densities of 5.0 and 10.0 mA cm^{-2}, and (c) voltage profiles of the HZPC electrode for the first Na deposition at current densities from 0.1 to 10.0 mA cm^{-1}.

Fig. S9a shows the voltage profiles of the bare Cu foil electrode at current densities from 0.1 to 10.0 mA cm^{-1}. The initial potential dips of the bare Cu foil electrode dramatically increase from –0.247 V (vs. Na^+/Na, 0.1 mA cm^{-1}) to −0.688 V (vs. Na^+/Na, 10.0 mA cm^{-1}). As the current density increased, the voltage profiles and overpotentials for Na deposition were not regularly controlled. Fig. S9b presents the FE-SEM images after the first Na deposition at current densities of 5.0 and 10.0 mA cm^{-2}. It can be seen that the morphology was not uniform at the high current densities. Fig. S9c shows the voltage profiles of the HZPC electrode at current densities from 0.1 to 10.0 mA cm^{-1}. The potential dips and overpotentials increased regularly as the current density increased. This phenomenon can be attributed to the role of Zn clusters on the porous carbon, which regulate the nucleation and growth of Na metal.

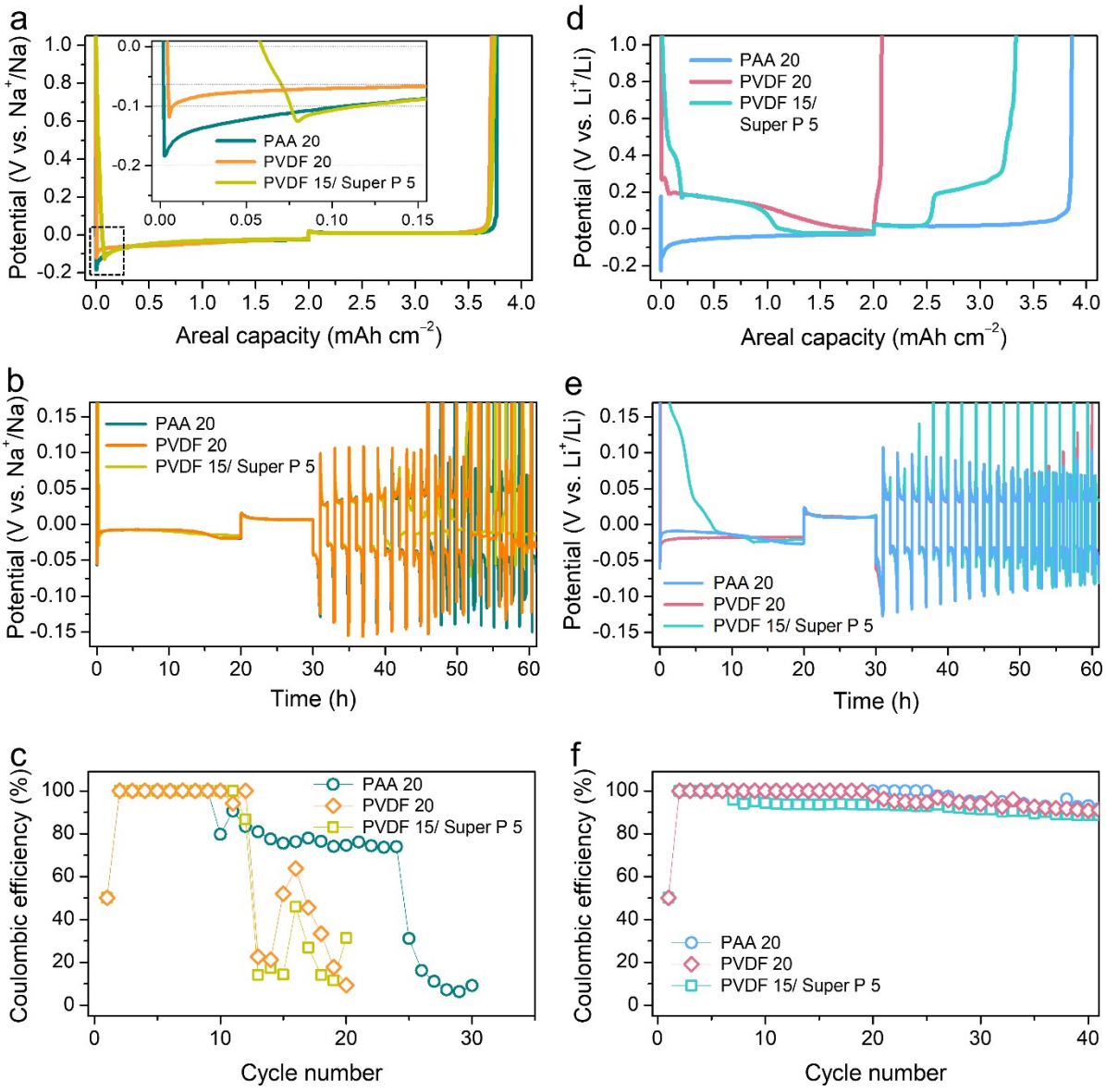

Fig. S10. Electrochemical properties of Zn metal powder electrodes using various binders and conducting material (the number means the percent ratio of the binder or activated carbon) for (a–c) Na metal and (d–f) Li metal plating/stripping. For the first cycle (a and d), a fixed amount of Na and Li (capacity: 2 mAh cm^{-2}) were plated and stripped at a current density of 0.1 mA cm^{-2}. For long-term cycling of the half-cells (b, c, e, and f), the first deposition and dissolution capacity were 2.0 mAh cm^{-2} and 1.0 mAh cm^{-2}, respectively, at a current density of 0.1 mA cm^{-2}. For subsequent metallic plating/stripping, the capacity was fixed at 1.0 mAh cm^{-2} at a current density of 1.0 mA cm^{-2}.

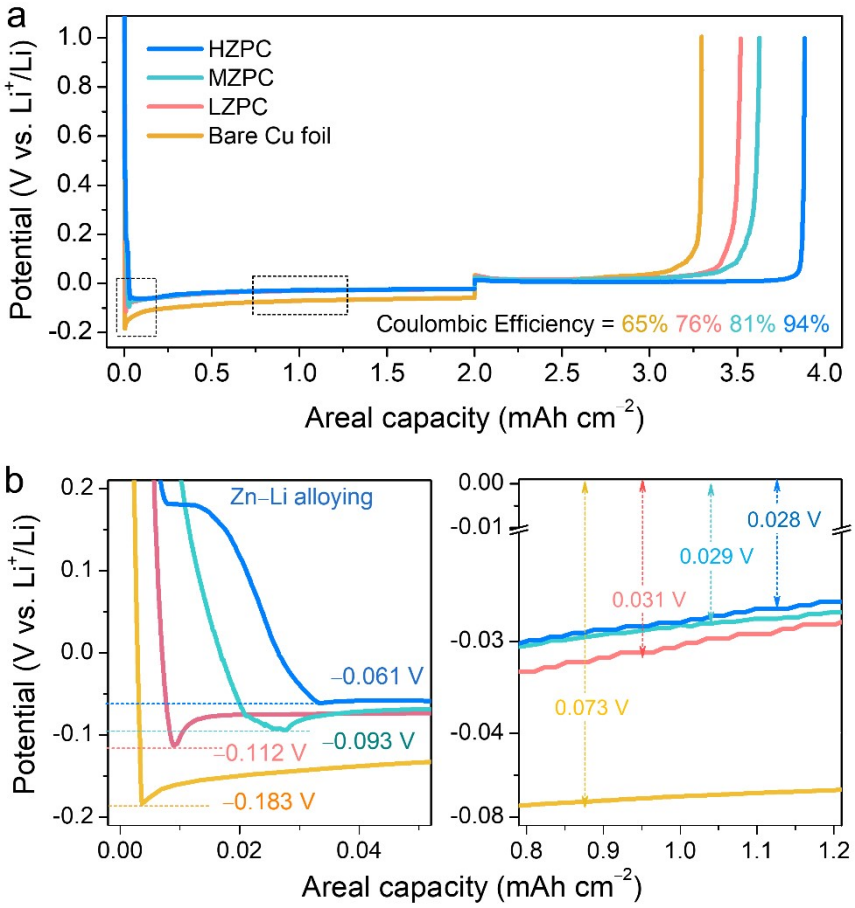

Fig. S11. (a) Galvanostatic voltage profiles during first Li metal plating/stripping at a current density of 0.1 mA cm^{-2} with a fixed areal capacity of 2.0 mAh cm^{-2} for all electrodes and (b) enlarged voltage profiles.

The initial Coulombic efficiencies of the HZPC, MZPC, LZPC, and bare Cu foil electrodes are 94%, 81%, 76%, and 65%, respectively. As similar to the Na storage, the HZPC electrode exhibits the highest efficiency possibly because of the Zn incorporation effect. Li-Zn alloying reactions during the first Li insertion process are observed for all the porous carbon electrodes, which indicates that the electrochemical Li-Zn alloying process shows fast kinetics compared to the Na-Zn alloying.

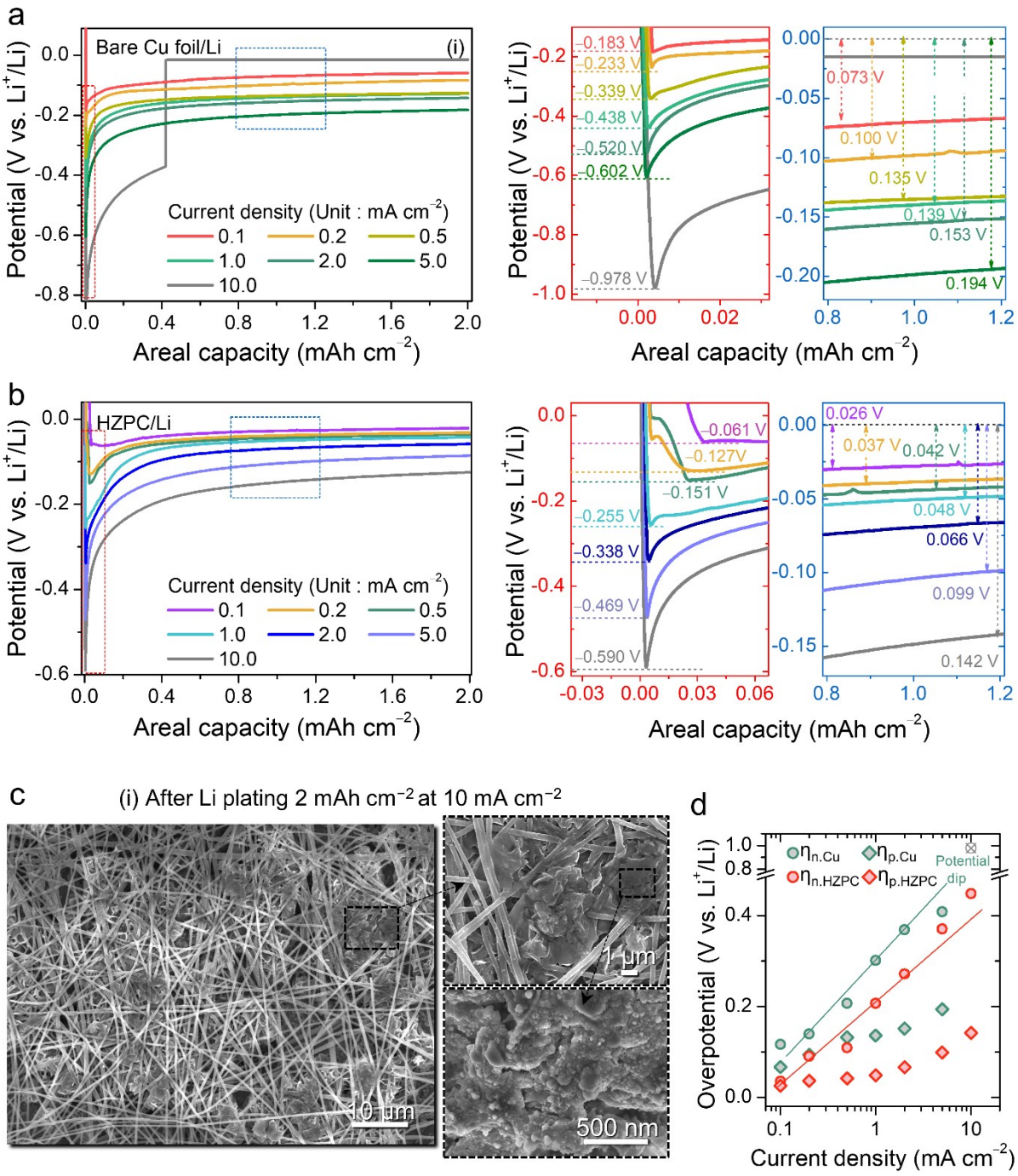

Fig. S12. Voltage profiles of the (a) bare Cu foil and (b) HZPC electrode for the first Li deposition at current densities from 0.1 to 10.0 mA cm^{-1}. (c) FE-SEM images after the first Li deposition at a current density of 10.0 mA cm^{-2}. (d) Li nucleation and plateau overpotentials at various current densities from 0.1 to 10.0 mA cm^{-2}.

Fig. S12a and b show the voltage profiles of the bare Cu foil and HZPC electrodes at current densities from 0.1 to 10.0 mA cm^{-1}. The initial potential dips of the bare Cu foil electrode significantly increase from −0.183 V (vs. Li^+/Li, 0.1 mA cm^{-1}) to −0.978 V (vs. Li^+/Li, 10.0 mA cm^{-1}). In the case of the HZPC electrode, the initial potential dips increase from −0.061 V (vs. Li^+/Li, 0.1 mA cm^{-1}) to −0.590 V (vs. Li^+/Li, 10.0 mA cm^{-1}). As a result, both η_n and η_p overpotentials for the HZPC electrode are lower at various current densities, which can be attributed to the electrochemical alloying reaction of Li-Zn during the first Li insertion. It should be noted that the electrochemical Li-Zn alloying reaction is beneficial to effectively reduce the nucleation barriers. Fig. S12c shows the FE-SEM images after the first Li deposition on the bare Cu foil electrode at a current density of 10.0 mA cm^{-2}. Li dendritic growth was observed on the Cu electrodes at the high current density. However, it was not observed in the HZPC electrode at the same current density.

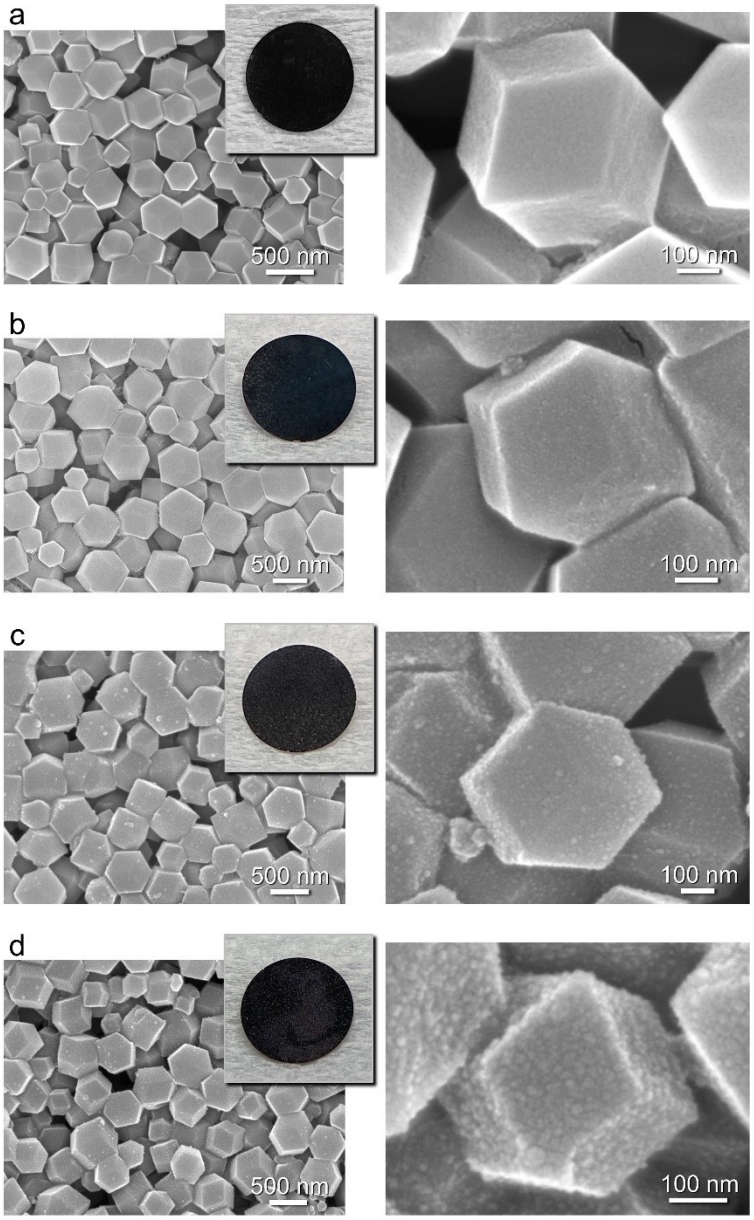

Fig. S13. Ex situ FE-SEM images (inset: photographs for electrodes, diameter = 12 mm) showing Na metal nucleation and growth mechanism during deposition at selected areal capacities of (a) 0.2, (b) 1.0, (c) 2.0, and (d) 4.0 mAh cm^{-2} for the HZPC electrodes.

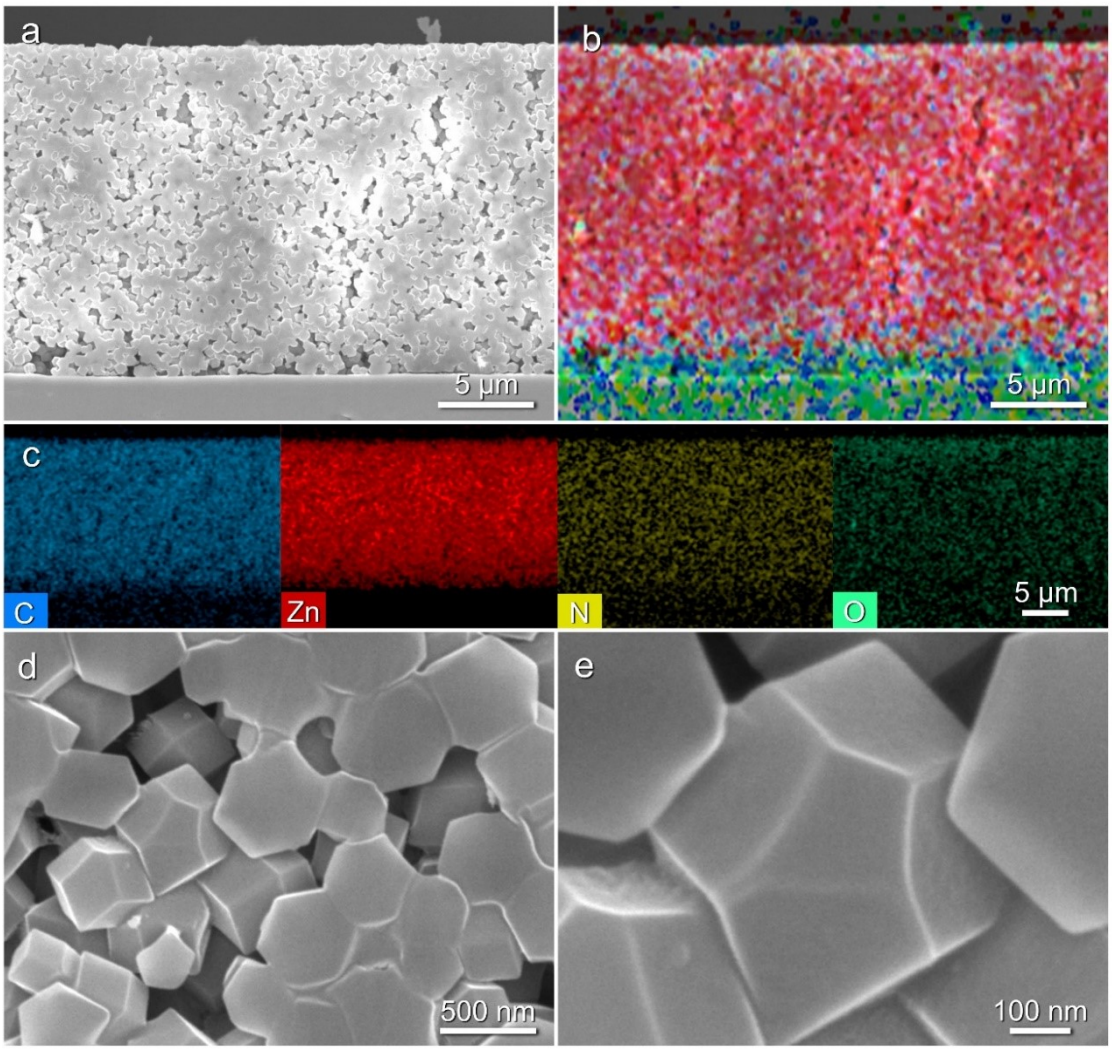

Fig. S14. Cross-sectional FE-SEM and EDS results of the pristine HZPC electrodes: (a) FE-SEM image, (b) EDS layered mapping image, (c) EDS elemental mapping results, and (d, e) enlarged FE-SEM images.

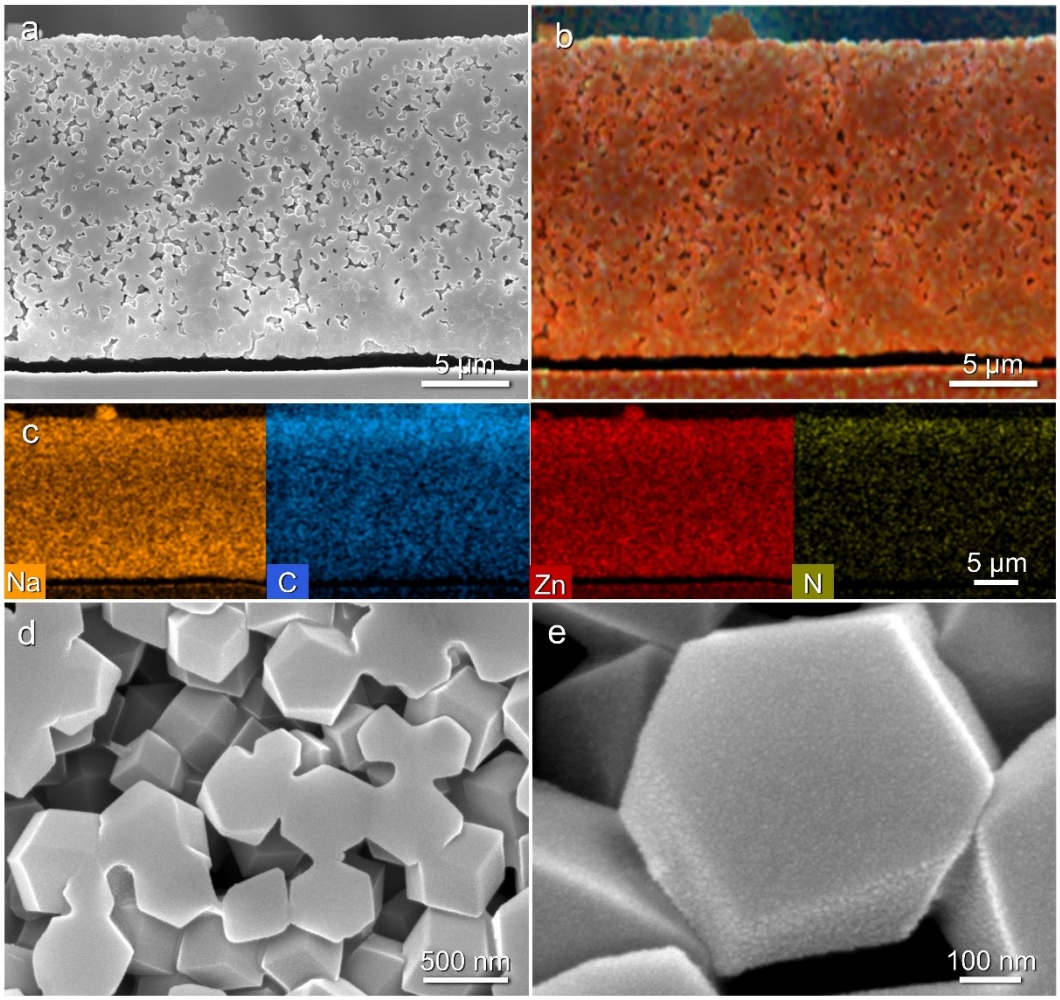

Fig. S15. Cross-sectional FE-SEM and EDS results of the charged HZPC electrodes (Na deposited for 2.0 mAh cm^{-2}): (a) FE-SEM image, (b) EDS layered mapping image, (c) EDS elemental mapping results, and (d, e) enlarged FE-SEM images.

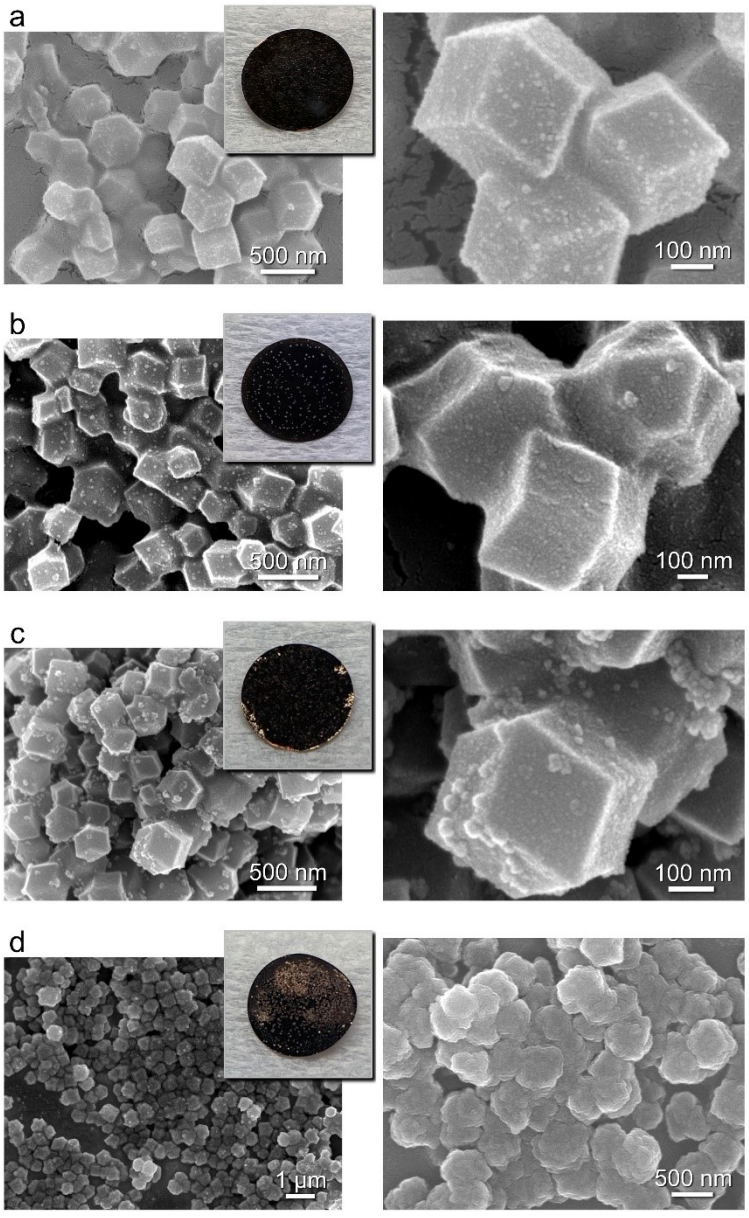

Fig. S16. Ex situ FE-SEM images (inset: photographs for electrodes, diameter = 12 mm) showing Li metal nucleation and growth mechanism during deposition at selected areal capacities of (a) 0.2, (b) 1.0, (c) 2.0, and (d) 4.0 mAh cm^{-2} for HZPC electrodes.

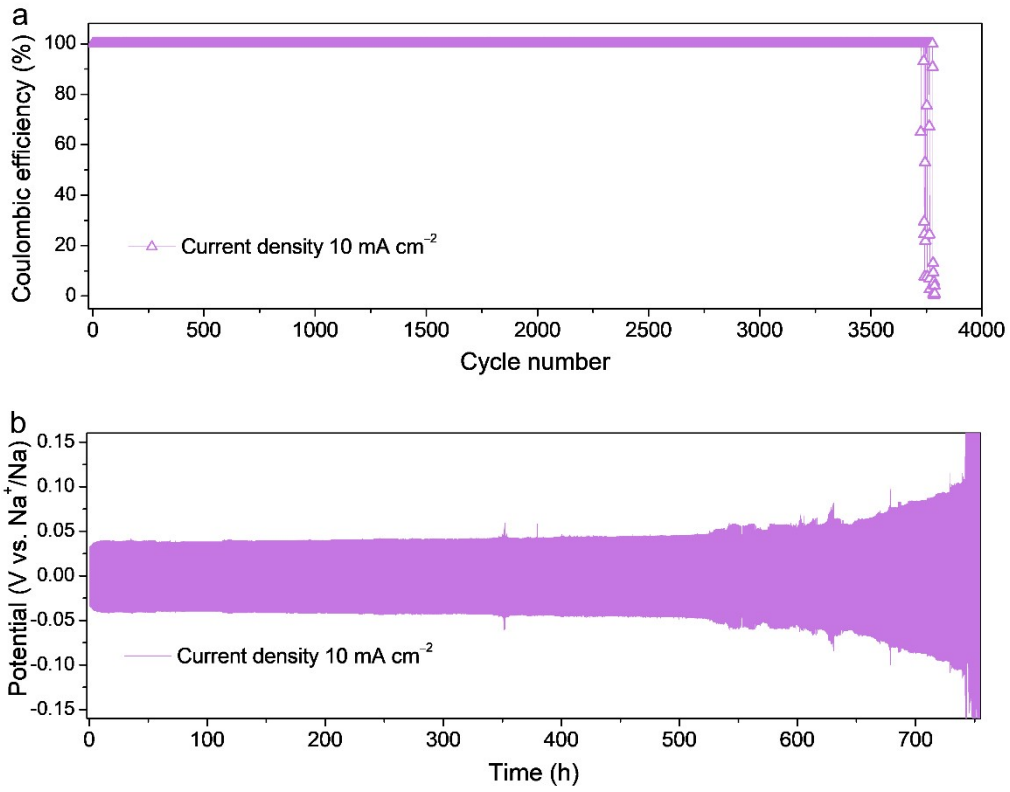

Fig. S17. Long-term cycling performance of the HZPC electrode for Na metal plating/stripping: (a) Coulombic efficiency upon cycling and (b) voltage profiles at a high current density of 10 mA cm^{-2} with fixed capacity of 1 mAh cm^{-2}.

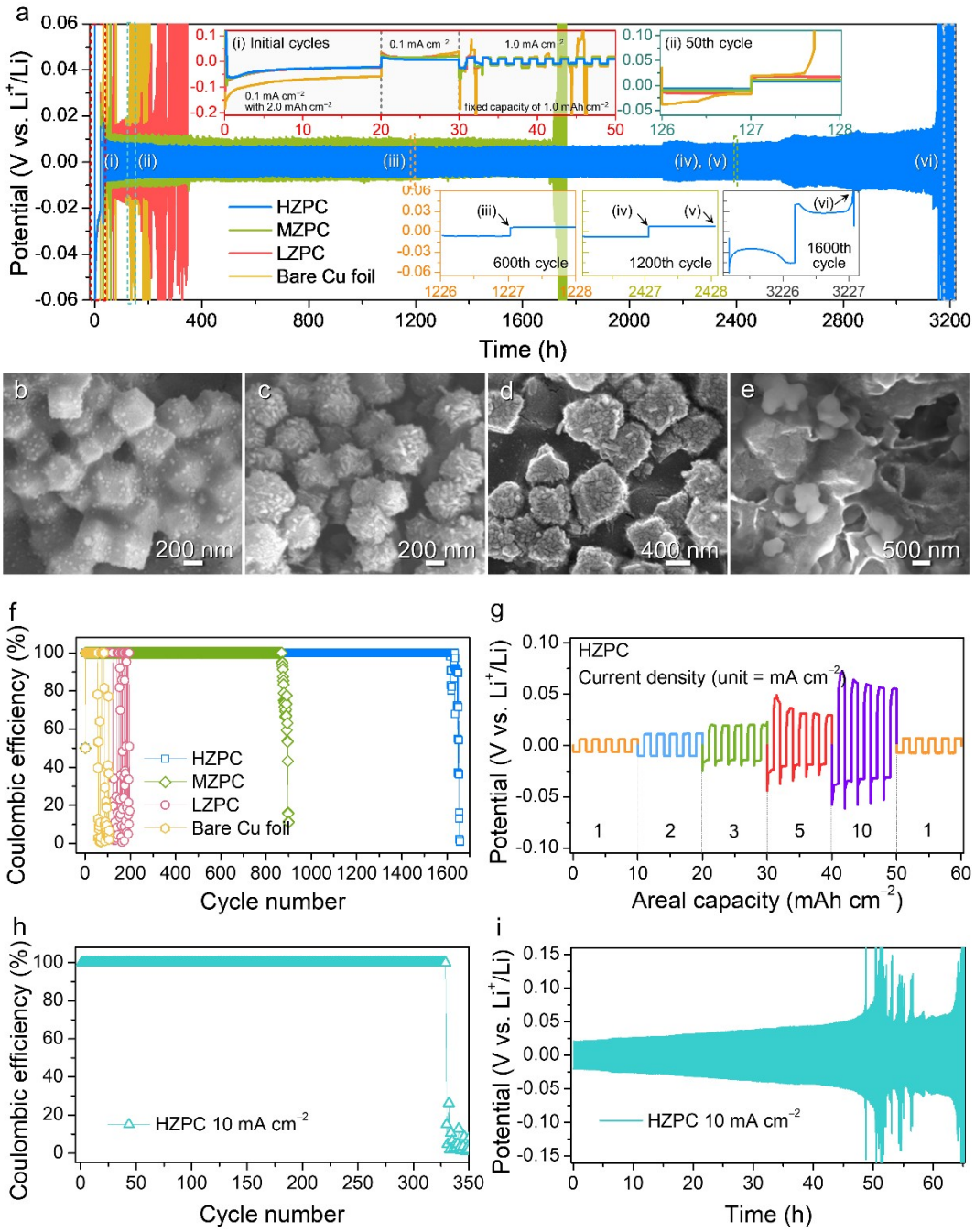

Fig. S18. Electrochemical performance comparison for all the Zn-containing porous carbon electrodes and bare Cu foil in the Li system: (a) Voltage profiles showing a stable cycle polarization at a current density of 1.0 mA cm^{-2} with a fixed capacity of 1.0 mAh cm^{-2}. The enlarged voltage profiles are presented in the inset. Ex situ FE-SEM images obtained after the (b) 600th dissolution, (c) 1200th deposition, (d) 1200th dissolution, and (e) 1600th dissolution. (f) Cycle and (g) rate performance of the HZPC electrode at various current densities of 1–10

mA cm^{-2}. (h) Cycle performance and (i) voltage profiles of the HZPC electrode at a current density of 10 mA cm^{-2}.

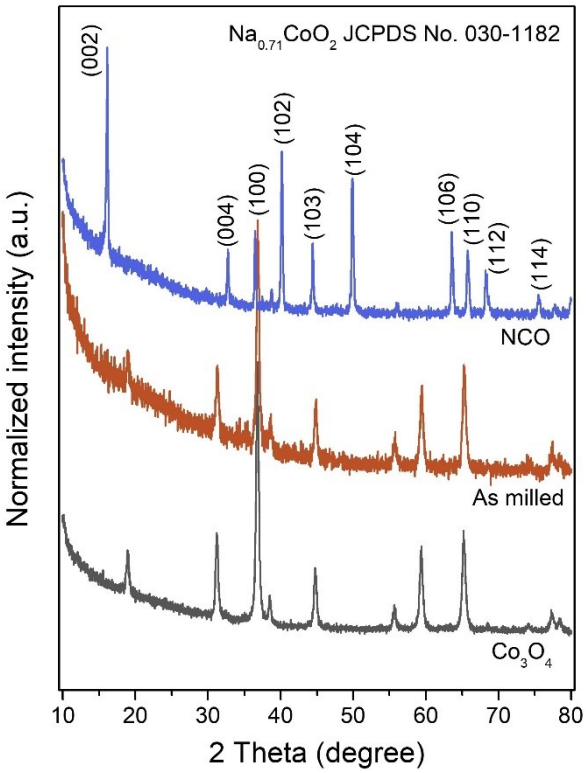

Fig. S19. XRD patterns of pristine Co_3O_4, as-milled precursors to NCO, and finally synthesized NCO.

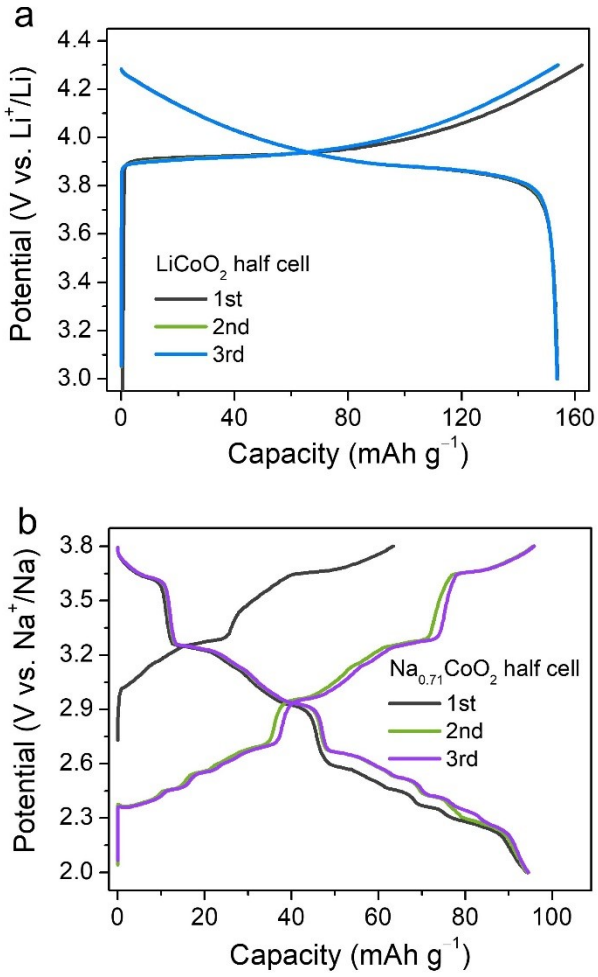

Fig. S20. Voltage profiles at a rate of 0.1 C for (a) $LiCoO_2$ cathode (Li half-cell, 1 C = 150 mA g^{-1}) and (b) $Na_{0.71}CoO_2$ cathode (Na half-cell, 1 C = 100 mA g^{-1}).

Table S2. Electrochemical performance comparison of the ZIF-derived electrodes.

Materials/ type of storage	Cycle performance Capacity/Coulombic efficiency: CE % (current density)	Full cell Capacity/retention efficiency: RE % (current density)	Ref.
Zn-containing porous carbon/ Na and Li metal batteries	Na metal: 1 mAh cm^{-2}/CE 99% over 2800 cycles (1.0 mA cm^{-2}) 1 mAh cm^{-2}/CE 99% over 3000 cycles (10.0 mA cm^{-2}) Li metal: 1 mAh cm^{-2}/CE 99% over 1600 cycles (1.0 mA cm^{-2}) 1 mAh cm^{-2}/CE 99% over 320 cycles (10.0 mA cm^{-2})	$Na_{0.71}CoO_2$ 99 mAh g^{-1}/RE 99% over 100 cycles (10 mA g^{-1}) 99 mAh g^{-1}/RE 99% over 100 cycles (100 mA g^{-1}) $LiCoO_2$ 155 mAh g^{-1}/RE 94% over 100 cycles (15 mA g^{-1}) 130 mAh g^{-1}/RE 95% over 100 cycles (150 mA g^{-1})	This study
ZnO/$ZnFe_2O_4$/C/ Li-ion battery	1390 mAh g^{-1}/CE 99% over 100 cycles (500 mA g^{-1}) 988 mAh g^{-1}/CE 99% over 100 cycles (2000 mA g^{-1})	-	S1
ZnO/N-doped CNT/ Li-ion battery	850 mAh g^{-1}/CE 99% over 200 cycles (100 mA g^{-1}) 300 mAh g^{-1}/CE 99% over 100 cycles (1000 mA g^{-1})	-	S2
Co/N-doped porous graphene/ Li-metal battery	1 mAh cm^{-2}/CE 99% over 300 cycles (1.0 mA cm^{-2}) 1 mAh cm^{-2}/CE 90% over 250 cycles (3000 mA cm^{-2})	$LiNi_{0.5}Co_{0.2}Mn_{0.3}O$ 135 mAh g^{-1}/RE 96% over 100 cycles (160 mA g^{-1})	S3
Zn-decorated and etching-treated porous carbon/ Li-metal battery	0.2 mAh cm^{-2}/CE 99% over 350 cycles (0.2 mA cm^{-2})	-	S4
Li-infused ZnO carbon/ Li-metal battery	1 mAh cm^{-2}/CE 99% over 200 cycles (1.0 mA cm^{-2}) 1 mAh cm^{-2}/CE 99% over 200 cycles (10.0 mA cm^{-2})	-	S5
S-doped Zn/Co in three-dimensional network carbon/ Na-ion battery	450 mAh g^{-1}/CE 99% over 100 cycles (100 mA g^{-1}) 225 mAh g^{-1}/CE 99% over 3000 cycles (5000 mA g^{-1})	$Na_3V_2(PO_4)_3$ 230 mAh g^{-1}/RE 84% over 50 cycles (100 mA g^{-1})	S6

MOF-199, ZIF-8/ Li and Na metal batteries	Li metal (ZIF-8): 1 mAh cm^{-2}/CE 99% over 300 cycles (1.0 mA cm^{-2}) Na metal (MOF-199): 1 mAh cm^{-2}/CE 80% over 26 cycles (1.0 mA cm^{-2})		S7
ZnNi porous carbon nanofiber/ Na metal battery	1 mAh cm^{-2}/CE 99% over 200 cycles (1.0 mA cm^{-2})	$Na_3V_2(PO_4)_3$ 75 mAh g^{-1}/RE 93% over 1000 cycles (118 mA g^{-1})	S8
N-doped porous carbon/ Na metal battery	1 mAh cm^{-2}/CE 99% over 400 cycles (1.0 mA cm^{-2}) 1 mAh cm^{-2}/CE 99% over 36 cycles (5.0 mA cm^{-2})	$Na_3V_2(PO_4)_2F_3$ 113 mAh g^{-1}/RE 90% over 100 cycles (60 mA g^{-1}) 86 mAh g^{-1}/RE 82% over 1000 cycles (1200 mA g^{-1})	S9

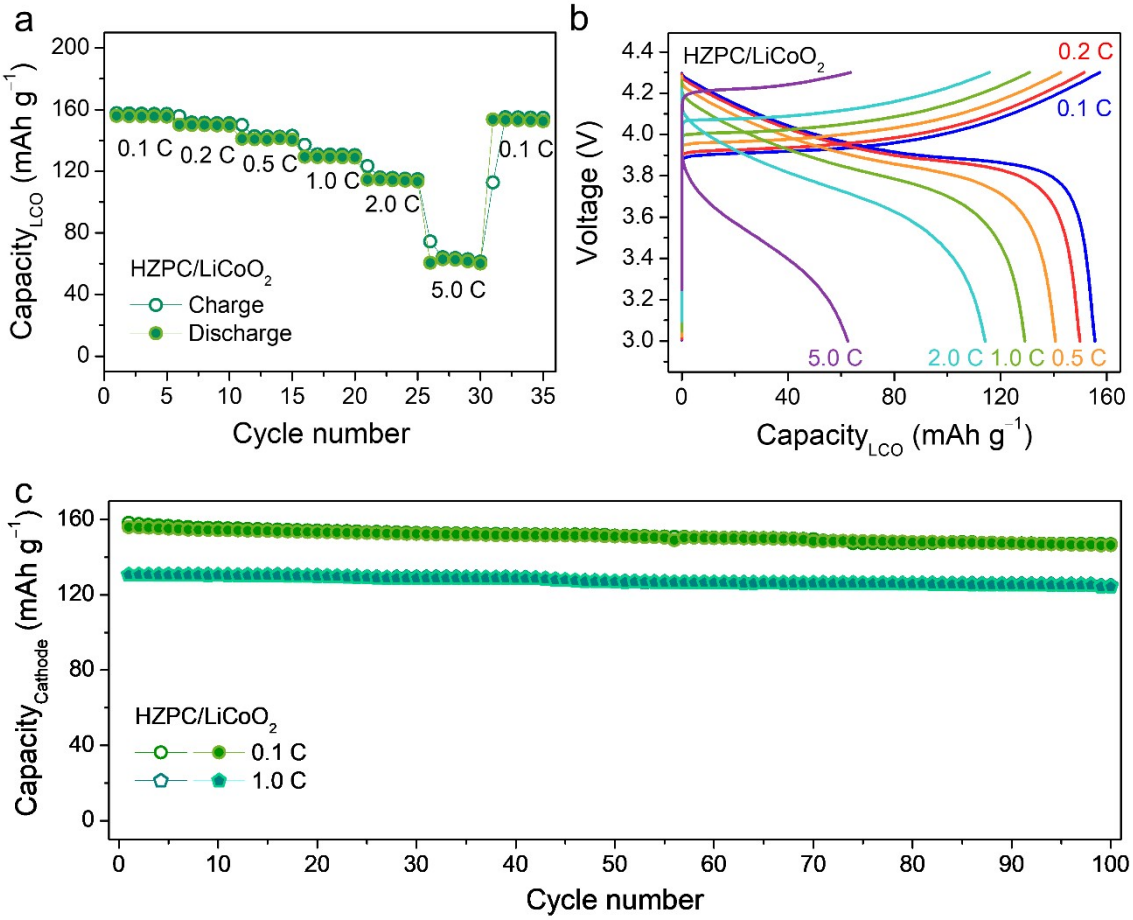

Fig. S21. HZPC/$LiCoO_2$ full cell test results (1 C = 150 mA g^{-1}): (a) Rate performance at various current densities of 0.1–5.0 C, (b) voltage profiles, and (c) cycle performance at the current densities of 0.1 and 1 C.

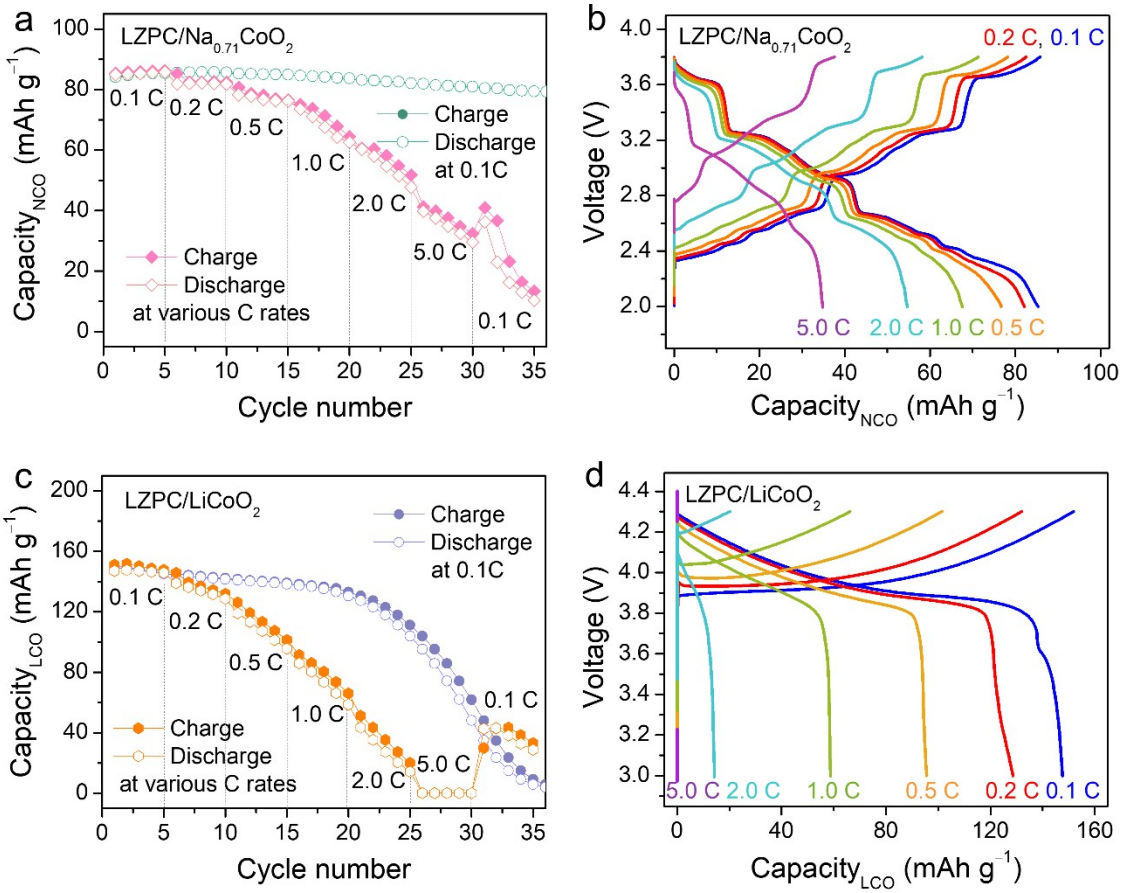

Fig. S22. Full cell test results of the LZPC electrode pairing with the $Na_{0.71}CoO_2$ and $LiCoO_2$ cathodes: (a) Cycle and rate performance, and (b) voltage profiles of the LZPC/$Na_{0.71}CoO_2$ cell at various rates. (c) Cycle and rate performance, and (d) voltage profiles of the LZPC/$LiCoO_2$ cell at various rates.

The full cells with the LZPC electrodes exhibited relatively higher overpotential and capacity fading in both Na and Li systems, compared to the full cells with the HZPC electrodes.

References

S1. F. Zou, X. Hu, Z. Li, L. Qie, C. Hu, R. Zeng, Y. Jiang and Y. Huang, *Adv. Mater.*, 2014, **26**, 6622–6628.

S2. H. Zhang, Y. Wang, W. Zhao, M. Zou, Y. Chen, L. Yang, L. Xu, H. Wu and A. Cao, *ACS Appl. Mater. Interfaces*, 2017, **9**, 37813–37822.

S3. T.-S. Wang, X. Liu, X. Zhao, P. He, C.-W. Nan and L.-Z. Fan, *Adv. Funct. Mater.*, 2020, **30**, 2000786.

S4. J. Kim, J. Lee, J. Yun, S.H. Choi, S.A. Han, J. Moon, J.H. Kim, J.-W. Lee and M.-S. Park, *Adv. Funct. Mater.*, 2020, **30**, 1910538.

S5. L. Wang, X. Zhu, Y. Guan, J. Zhang, F. Ai, W. Zhang, Y. Xiang, S. Vijayan, G. Li, Y. Huang, G. Cao, Y. Yang and H. Zhang, *Energy Storage Mater.*, 2018, **11**, 191–196.

S6. W. Zhong, X. Lv, Q. Chen, M. Ren, W. Liu, G. Li, J. Yu, M. Li, Y. Dai and L. Wang, *ACS Appl. Mater. Interfaces*, 2019, **11**, 37850–37858.

S7. J. Qian, Y. Li, M. Zhang, R. Luo, F. Wang, Y. Ye, Y. Xing, W. Li, W. Qu, L. Wang, L. Li, Y. Li, F. Wu and R. Chen, *Nano Energy*, 2019, **60**, 866–874.

S8. N. Mubarak, M. Ihsan-Ul-Haq, H. Huang, J. Cui, S. Yao, A. Susca, J. Wu, M. Wang, X. Zhang, B. Huang and J.-K. Kim, *J. Mater. Chem. A*, 2020, **8**, 10269–10282.

S9. Y. Xie, J. Hu, Z. Han, T. Wang, J. Zheng, L. Gan, Y. Lai and Z. Zhang, *Energy Storage Mater.*, 2020, **30**, 1–8.